

Broadband radio-frequency spectrum analysis in spectral-hole-burning media

Max Colice, Friso Schlottau, and Kelvin H. Wagner

We demonstrate a 20 GHz spectrum analyzer with 1 MHz resolution and >40 dB dynamic range using spectral-hole-burning (SHB) crystals, which are cryogenically cooled crystal hosts lightly doped with rare-earth ions. We modulate a rf signal onto an optical carrier using an electro-optic intensity modulator to produce a signal beam modulated with upper and lower rf sidebands. Illuminating SHB crystals with modulated beams excites only those ions resonant with corresponding modulation frequencies, leaving holes in the crystal's absorption profile that mimic the modulation power spectrum and persist for up to 10 ms. We determine the spectral hole locations by probing the crystal with a chirped laser and detecting the transmitted intensity. The transmitted intensity is a blurred-out copy of the power spectrum of the original illumination as mapped into a time-varying signal. Scaling the time series associated with the transmitted intensity by the instantaneous chirp rate yields the modulated beam's rf power spectrum. The homogeneous linewidth of the rare-earth ions, which can be <100 kHz at cryogenic temperatures, limits the fundamental spectral resolution, while the medium's inhomogeneous linewidth, which can be >20 GHz, determines the spectral bandwidth. © 2006 Optical Society of America
OCIS codes: 070.1170, 160.5690.

1. Conventional Radio-Frequency Spectrum Analysis

Future advances in rf technology will require new techniques for processing extremely broadband signals. Applications such as radar and electronic warfare require large dynamic range and fine spectral resolution in addition to broad bandwidth. Signal processors such as spectrum analyzers also need a high probability of intercept to acquire frequency-hopping or aperiodically pulsed signals. We demonstrate a spectrum analyzer based on spectral hole burning (SHB) with a 20 GHz bandwidth, resolution of 1 MHz, and operation with unity probability of intercept. Our spectrum analyzer uses optical techniques to perform spectral discrimination and low-bandwidth electronics for detection and postprocessing. It has a time-bandwidth product of 20,000, which is, to our knowledge, the highest of any 1D analog spectrum analyzer.

Scanning superheterodyne spectrum analyzers, the most common type of conventional spectrum an-

alyzer, beat rf inputs against a local oscillator (LO) and detect the filtered difference, or intermediate, frequency (IF) between the rf input and the LO.^{1,2} Sweeping the LO frequency changes the amount of frequency translation experienced by the rf input. In other words, the IF (i.e., the translated rf input) sweeps by the IF filter at the LO sweep rate. Electronics behind the IF filter process pieces of the rf input spectrum sequentially, displaying the pieces from left to right on a video display. Because the LO sweeps across the frequency band in a sequential fashion, it is difficult to detect frequency-hopping or pulsed signals with scanning superheterodyne spectrum analyzers. If a pulsed signal happens to be off when the LO sweeps by, the spectrum analyzer will not record an IF blip, so the pulsed signal will slip by undetected.

Real-time spectrum analyzers use digital signal processing to fast Fourier transform (FFT) temporal snapshots of a subband of the rf spectrum, eliminating some of the problems associated with sweeping LOs.³ They amplify and downconvert a selected rf subband with an analog front end before digitizing captured data with analog-to-digital converters (ADC). A digital signal processing engine stores digitized data as frames, initiating a FFT once the real-time spectrum analyzer acquires a predetermined amount of data. Because ADCs with high dynamic range can operate only over narrow bandwidths, the bandwidth of real-time spectrum analyzers is limited to around 100 MHz, the maximum ADC bandwidth.

When this research was performed, all the authors were with the Optoelectronic Computing Systems Center, Department of Electrical and Computer Engineering, University of Colorado at Boulder, Boulder, Colorado 80309. F. Schlottau is now with InPhase Technologies, 2000 Pike Road, Longmont, Colorado 80501. M. Colice's e-mail address is colice@colorado.edu.

Received 5 December 2005; accepted 17 April 2006; posted 19 May 2006 (Doc. ID 66415).

0003-6935/06/256393-16\$15.00/0

© 2006 Optical Society of America

Conventional optical signal processing exploits the inherent spatial parallelism of optics to avoid problems associated with both sweeping LOs and narrowband ADCs. Most previous optical techniques transform rf inputs—modulations in time—into spatial modulation, which can be processed by propagation through an appropriately designed system of lenses and modulators.⁴ Space-integrating acousto-optic spectrum analyzers use the traveling-wave nature of acoustic propagation to deflect an incident optical beam at angles proportional to the rf frequencies driving the acoustic wave.⁵ A lens Fourier transforms deflected beams to produce a spatial version of the signal spectrum, which can be detected using a CCD or similar 1D detector array. Acoustic wave generation and attenuation limit the bandwidth of these devices to approximately 1 GHz. In contrast, SHB media can process signal bandwidths of up to 200 GHz (Ref. 6) using spectral parallelism while retaining all the advantages of spatial parallelism as exploited by acousto-optic spectrum analyzers.

In Section 2 we discuss SHB processors in general and several different types of rf spectrum analyzer based on SHB media. We then present a theoretical analysis and experimental demonstration of our spectrum analyzer, which processes 20,000 spectral bins in a single spot. We use third-order perturbation theory to determine the fundamental resolution limit of spectrum analysis processes in SHB media in Section 3. In Section 4 we use our perturbation theory result to explain the spectral recovery algorithm and contrast spectral recovery with the multiply–convolve–multiply transform described in Section 2. We then examine the relationship between incident power and hole depth in Sections 5 and 6 to determine dynamic range performance of SHB spectrum analyzers. We discuss our experiment and results in Sections 7 and 8, concluding with comments on bandwidth, resolution, and dynamic range.

2. Radio-Frequency Spectrum Analysis in Spectral-Hole-Burning Media

SHB media support spectral parallelism in addition to spatial parallelism, giving us four dimensions (three spatial and one spectral) in which to process information. SHB media are rare-earth ions such as Tm^{3+} or Er^{3+} doped into crystal hosts such as YAG or LiNbO_3 . The rare-earth ions act as dipole oscillators with homogeneous linewidth $1/T_2$, which can be under 100 kHz for cryogenically cooled crystals.⁷ Inhomogeneous variations in the ions' local environments shift the resonance frequency of each oscillator. These variations spread the resonances over an inhomogeneous linewidth $1/T_2^*$, which can be up to 200 GHz in materials such as $\text{Er}^{3+}:\text{LiNbO}_3$.⁶ Illuminating SHB crystals at frequencies in the inhomogeneous band induces transitions from the ground state to the excited state for resonant ions, leaving spectral holes in the absorption band at the resonant frequencies. Spectral holes decay at a rate given by an excited

state lifetime T_1 , which is about 10 ms in Tm^{3+} - and Er^{3+} -doped crystals.

Because SHB media have a narrow homogeneous linewidth and a broad inhomogeneous linewidth, they can discriminate between different spectral components of incident fields. Records of this spectral discrimination, confined to the spot illuminated by the incident field, persist for the excited state lifetime. A single SHB crystal can accommodate hundreds of spots, each with T_2^*/T_2 spectral bins. For example, a 10 mm \times 10 mm \times 5 mm crystal with 200 GHz inhomogeneous linewidth and 100 kHz linewidth could accommodate 5×10^9 spatial-spectral bins, assuming 2500 spots of 100 μm diameter. Mossberg⁸ first proposed exploiting the spatial-spectral discrimination and lifetime characteristics of SHB media to perform rewritable optical data storage in 1982. Since then, other groups have proposed and demonstrated correlators,^{9–11} radar range finders,¹² true-time-delay processors,¹³ and spectrum analyzers^{14–16} built around the 4D processing capabilities of SHB media.

Because all the information in a rf power spectrum is contained in a 1D vector (power variation with frequency), we can perform rf spectrum analysis in SHB media using several different methods. Researchers at Centre Nationale de la Recherche Scientifique (CNRS) in France recently demonstrated a spectrum analyzer that copies the functionality of a Bragg cell into a SHB crystal with a set of angle-multiplexed gratings programmed into the crystal.¹⁷ Each grating corresponds to a particular frequency bin, as in an acousto-optic spectrum analyzer, but the grating configuration can be configured dynamically without the frequency limitations imposed by acoustic wave generation or attenuation. The gratings diffract different spectral components of incident beams at different angles; a Fourier lens focuses the diffracted beams onto an array of detectors. Each detector monitors a different frequency bin by sensing the presence of incident light. This system's major advantage lies in its rapid reconfigurability; however, the programming of gratings typically requires acousto-optic deflectors, which restricts the number of gratings to the space–bandwidth product of the deflectors. Proposed 2D configurations for writing spatial gratings could exceed this limitation.¹⁴

SHB crystals record time-domain interference of incident pulses as spectral gratings, as long the delay between pulses is less than the coherence time, T_2 . Diffractions off these gratings, also known as photon echoes, must obey causality conditions imposed by the time ordering of the programming pulses.¹⁸ Another scheme developed at CNRS for performing spectrum analysis in SHB media uses spectral gratings to perform the multiply–convolve–multiply chirp transform algorithm,¹⁹

$$S(\omega = 2\pi\kappa t) = [s(t)\exp(-i\pi\kappa t^2) * \exp(i\pi\kappa t^2)] \times \exp(-i\pi\kappa t^2), \quad (1)$$

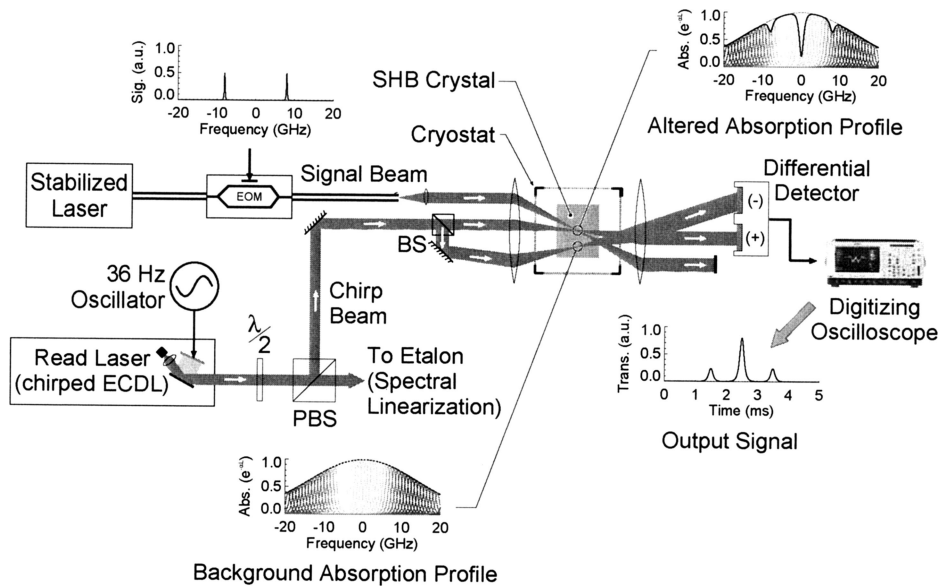


Fig. 1. Write-read process for spectrum analysis in SHB crystals. The signal beam propagates through an EOM, which is driven by the rf signal of interest, before being focused into the crystal. It burns the rf signal spectrum into the crystal's absorption profile. A chirped read beam probes the altered absorption profile before striking the (+) port of a differential detector. A chirped background beam probes the crystal's background absorption profile before striking the (-) port of the differential detector. The digitizing oscilloscope records changes in transmitted intensity as a map of the signal power spectrum.

where $s(t)$ is the signal, $S(\omega)$ is the signal spectrum, κ is the chirp rate, and $*$ indicates the convolution operation. The SHB crystal records the time-domain interference of a δ -like pulse followed less than T_2 seconds later by a chirp as a spectral fringe pattern confined to a single spot. The spectral fringe pattern is the Fourier transform of the convolution of the two pulses, i.e., $\mathcal{F}\{\delta(t) * \exp(i\pi\kappa t^2)\}$, where \mathcal{F} indicates the Fourier transform operation. Illuminating the grating with a chirp modulated by signal $s(t)$ produces a photon echo with an envelope $S(2\pi\kappa t)\exp(i\pi\kappa t^2)$. Detecting the photon echo yields the signal power spectrum $|S(2\pi\kappa t)|^2$ as mapped into the spectral domain by the chirp rate. The writing of spectral gratings requires temporal separation between pulses, so the chirp-transform spectrum analyzer cannot operate all the time, reducing its probability of intercept.

Instead of programming spatially or temporally multiplexed gratings into the material, we simply illuminate a single spot in a SHB crystal with a modulated signal beam.^{16,20,21} The signal beam engraves spectral holes into the absorption profile of the material at frequencies corresponding to the signal spectrum. These holes persist in the crystal for the excited state lifetime. We map the frequencies of the spectral holes by probing the absorption profile with a low-power chirp. As the chirp sweeps across a hole, its transmitted intensity increases in proportion to the hole depth. The transmitted intensity is proportional to the signal power spectrum mapped into time by the instantaneous chirp frequency, $|S(2\pi\kappa t)|^2$. By mapping the instantaneous chirp frequency to the temporal coordinate of the transmitted power, we determine the power spectrum of the high-bandwidth rf signals. The crystal's inhomogeneous linewidth

fixes the maximum signal bandwidth, and the homogeneous linewidth determines the resolution limit. For $\text{Tm}^{3+}:\text{YAG}$ crystals with $1/T_2^* = 20$ GHz and $1/T_2 \approx 100$ kHz, this translates to a time-bandwidth product of up to 200,000. Newly developed disorder crystals such as $\text{Er}^{3+}:\text{LiNbO}_3$ have bandwidths up to 200 GHz and $1/T_2 < 100$ kHz,⁶ suggesting time-bandwidth products in excess of 2×10^6 .

We previously demonstrated a low-bandwidth spectrum analyzer based on this technique that used a single acousto-optic modulator to write and then read an engraved pattern of spectral holes.¹⁶ This system suffered from two major drawbacks: (i) it relied on acousto-optic modulation, limiting system bandwidth, and (ii) it performed write and read operations in sequence, so it could miss pulsed signals. Pulsed or hopping signals can be extremely difficult to detect, and SHB crystals are ideal receivers because they record over all frequencies in a broad band for as long as they are illuminated. Using a temporally sequenced write-read process effectively turns the spectrum analyzer off during the read operation, so pulsed signals can slip by undetected.

We remedy these defects by replacing the acousto-optic modulator with an electro-optic modulator (EOM) and introducing a second beam to read the signal spectrum, as shown in Fig. 1. Off-the-shelf EOMs have bandwidths of up to 40 GHz, and both LiNbO_3 and polymer EOMs have been demonstrated with bandwidths of 100 GHz or more.^{22,23} SHB spectrum analyzers can also process signals well beyond the 3 dB bandwidth of the EOM by using appropriate postprocessing to account for the roll off of the EOM frequency response (and incurring a sensitivity penalty at high frequencies). We could also tune the laser

frequency to the side of the absorption maximum, using the inhomogeneous band shape to counterbalance EOM roll-off.

We perform simultaneous reading and writing by introducing a separate read beam, multiplexing the write and read operations angularly rather than temporally while still addressing the same spot. Because write and read processes occur simultaneously, the spectrum analyzer operates with unity probability of intercept. Read operations do not affect write processes so long as the read beam is of sufficiently low (submilliwatt) power and has a known amplitude envelope.

Some sensing applications require extremely low latency times, requiring fast and frequent interrogation of spectral holes. The spectral recovery algorithm developed by Chang *et al.*³⁰ eliminates the chirp-rate limits associated with resolution and dwell time, enabling relatively fast readout. Another way to decrease latency is to use multiple beams to read a single spot in the crystal. One option is to interrogate a single spot with angularly multiplexed beams, each of which chirps over a different subband. Another alternative is to interrogate the spot with a gigahertz-spaced frequency comb from a mode-locked laser.²⁴ Modulating the comb with a low-bandwidth chirp by double passing it through an acousto-optic modulator would sweep each comb order over a different rf subband without introducing angular scanning. Focusing the modulated comb into the crystal would interrogate all the subbands without spatial multiplexing. The comb orders can be separated with a fixed grating or a tilted etalon before being focused onto dedicated detectors. Such a spectrum analyzer could process over 200 GHz of bandwidth with under 100 kHz of resolution with latency times of the order of microseconds.

3. Perturbation Theory Limits on Resolution

Up to this point we have represented SHB crystals as ensembles of narrowband receivers without considering the dynamics of the interaction between incident beams and SHB media. Here we use perturbation theory to develop a formal description of this interaction. We start by assuming a set of incident fields $E_k(t)$ that drive the off-diagonal element ρ_{12} of the density matrix characterizing the coherence between the ground and the excited states of the medium. Off-diagonal density matrix elements describe both coherence between population levels and time evolution of state populations, which are given by the on-diagonal elements ρ_{11} and ρ_{22} . We relate ρ_{12} to the macroscopic material polarization, which, in turn, determines the output field as given by Maxwell's equations.²⁵

Following Mitsunaga and Brewer,¹⁸ we approximate interactions between the incident fields and the SHB media by using third-order perturbation theory to write a set of causal time-domain integrals for the expectation value of the off-diagonal density matrix element responsible for the diffracted field:

$$\begin{aligned} \langle \rho_{12}(t) \rangle = & \mathcal{D} \int_{-\infty}^t dt_3 \int_{-\infty}^{t_3} dt_2 \int_{-\infty}^{t_2} dt_1 E_3(t_3) E_2(t_2) E_1^*(t_1) \\ & \times \exp[-(t - t_3 + t_2 - t_1)/T_2] \\ & \times \exp[-(t_3 - t_2)/T_1] \\ & \times \delta(t_2 - t_1 + t_3 - t), \end{aligned} \quad (2)$$

where angled brackets indicate an average over frequency detuning. We take the time ordering to be $t_1 < t_2 < t_3 < t$ and define the proportionality constant $\mathcal{D} = -4i\sqrt{\pi}w_{\text{eq}}|\mu_{12}|^2/[(1/T_2^*)\hbar^3]$. In this expression, the equilibrium population inversion is $w_{\text{eq}} = \rho_{22} - \rho_{11} = -1$ for optical transitions, μ_{12} is the dipole moment, and \hbar is Planck's constant. The integrals are written using the rotating wave approximation to transform the problem into a reference frame rotating at the angular frequency of the incident wave.²⁶ The rotating wave approximation means we consider only the detuning or difference in frequencies. It also allows us to neglect terms associated with harmonics of the angular frequency.

The time-domain integrals given in Eq. (2) provide a good description of photon echoes and the time-domain manifestation of spectral gratings, but do not lend much insight into frequency-domain operations such as spectrum analysis. By defining $\tilde{E}(\omega) = \mathcal{F}\{E(t)\}$, we can Fourier transform Eq. (2) to get the frequency-domain integrals¹⁶

$$\begin{aligned} \langle \rho_{12}(t) \rangle = & \mathcal{D} \int_{-\infty}^{\infty} d\omega_3 \int_{-\infty}^{\infty} d\omega_2 \int_{-\infty}^{\infty} d\omega_1 \tilde{E}_3(\omega_3) \tilde{E}_2(\omega_2) \\ & \times \tilde{E}_1^*(\omega_1) \exp[i(\omega_3 + \omega_2 - \omega_1)t] \\ & \times \gamma_1(\omega_2 - \omega_1) \gamma_2(\omega_3 + \omega_2 - 2\omega_1), \end{aligned} \quad (3)$$

where the excited state lifetime is described by a convolution with the Lorentzian

$$\gamma_1(\omega_2 - \omega_1) = \frac{1}{(1/T_1) + i(\omega_2 - \omega_1)}, \quad (4)$$

and the coherence time is described by a convolution with the Lorentzian

$$\gamma_2(\omega_3 + \omega_2 - 2\omega_1) = \frac{1}{(2/T_2) + i(\omega_3 + \omega_2 - 2\omega_1)}. \quad (5)$$

The integrals in Eq. (3) are simply convolutions of the spectral domain products with the two Lorentzians.

Equation (3) represents the causal nature of Eq. (2) more compactly and without introducing any additional approximations. The Lorentzians in Eqs. (4) and (5) fully account for the causality embodied in the time ordering of Eq. (2), since a complex Lorentzian is the Fourier transform of an exponential decay and a Heaviside step function, which embodies the time ordering. The Lorentzian in Eq. (5) is of width $2/T_2$ rather than $1/T_2$ because the coherence time mani-

fects itself twice, once during the interaction of $\tilde{E}_1^*(\omega_1)$ and $\tilde{E}_2(\omega_2)$, and again during the interaction between $\tilde{E}_3(\omega_3)$ and the emitted field, which is proportional to $\langle \rho_{12}(t) \rangle$.

Choosing the fields correctly allows us to use frequency-domain integrals to predict the spectral performance of SHB spectrum analyzers. We define incident signals as degenerate fields $E_1(t) = E_2(t) = a(t)\exp(i\omega_0 t)$, where $a(t)$ is the envelope from the rf modulation and ω_0 is the optical carrier frequency. The carrier frequency can be tuned within or to the edge of the SHB crystal's inhomogeneous bandwidth, so long as at least one of the rf sidebands remains within the absorption profile. We describe the engraving process in the frequency domain by using the notation $\tilde{E}_1(\omega) = \tilde{E}_2(\omega) = S(\omega)$ and substituting into Eq. (3).

We use a chirp beam $E_3(t) = (2C\tau\sqrt{\kappa})\exp(i\pi/4)\exp[i(\omega_c t + \pi\kappa t^2)] * \delta(t - t_0)$ to probe the altered absorption profile. In this case, ω_c is the chirp center frequency and $\kappa = b + [i/(\pi\tau^2)]$, where b is the chirp rate in Hz/s, and τ is the width of the Gaussian amplitude envelope in seconds. We also include a constant amplitude weight C and a time shift of t_0 , as given by the convolution with the δ function. We write the chirp in the frequency domain as $\tilde{E}_3(\omega) = C \exp[i(\omega - \omega_c)^2/(4\pi\kappa)]\exp(i\omega t_0)$. Substituting the degenerate signal fields and the chirp field into Eq. (3) yields

$$\begin{aligned} \langle \rho_{12}(t) \rangle = & \mathcal{D} \int_{-\infty}^{\infty} d\omega_3 \int_{-\infty}^{\infty} d\omega_2 \int_{-\infty}^{\infty} d\omega_1 C \\ & \times \exp[i(\omega_3 - \omega_c)^2/(4\pi\kappa)] \exp(i\omega_3 t_0) \\ & \times S(\omega_2) S^*(\omega_1) \exp[i(\omega_3 + \omega_2 - \omega_1)t] \\ & \times \gamma_1(\omega_2 - \omega_1) \gamma_2(\omega_3 + \omega_2 - 2\omega_1). \end{aligned} \quad (6)$$

Recalling that $T_1 = 10$ ms ($\gg T_2 \approx 10$ μ s), we approximate the Lorentzian in Eq. (4) as $\delta(\omega_2 - \omega_1)$, integrate over ω_1 , and rearrange the resulting integrals to get

$$\begin{aligned} \langle \rho_{12}(t) \rangle = & \mathcal{D} \int_{-\infty}^{\infty} \left[\int_{-\infty}^{\infty} |S(\omega_2)|^2 \gamma_2(\omega_3 - \omega_2) d\omega_2 \right] \\ & \times C \exp[i(\omega_3 - \omega_c)^2/(4\pi\kappa)] \\ & \times \exp[i\omega_3(t + t_0)] d\omega_3. \end{aligned} \quad (7)$$

The signal power spectrum, $|S(\omega_2)|^2$, determines the locations and depths of the spectral holes, while the Lorentzian line shape of the ionic resonances fixes the holes' shapes. Spectral holes filter the incident chirp, $\exp[i(\omega_3 - \omega_c)^2/(4\pi\kappa)]$, to produce changes in the time-averaged density matrix element $\langle \rho_{12}(t) \rangle$, which determines the transmitted field. We have previously used the method of stationary phase¹⁶ to show that integrating Eq. (7) yields the correlation of the signal power spectrum, $|S(\kappa t)|^2$, with a scanning Lorentzian in a coordinate system determined by chirp rate κ .

Here, we choose to recognize that the integral over ω_2 in Eq. (7) is the convolution of the Lorentzian with the signal power spectrum. This convolution is the operation that fundamentally limits the resolution of SHB spectrum analyzers to $2/T_2$. We introduce a new variable, $H(\omega)$, as a shorthand for signal power spectra as recorded by SHB crystals:

$$H(\omega_3) = \int_{-\infty}^{\infty} |S(\omega_2)|^2 \gamma_2(\omega_3 - \omega_2) d\omega_2. \quad (8)$$

Rewriting Eq. (7) using our shorthand notation gives

$$\begin{aligned} \langle \rho_{12}(t) \rangle = & \mathcal{D} \int_{-\infty}^{\infty} H(\omega_3) C \exp[i(\omega_3 - \omega_c)^2/(4\pi\kappa)] \\ & \times \exp[i\omega_3(t + t_0)] d\omega_3. \end{aligned} \quad (9)$$

We use H to denote recorded power spectra so we can better point out the analogy to linear systems. In this analogy, SHB crystals act as programmable filters. Incident signals determine the filter shape, which we characterize with a transfer function, $H(\omega)$. Chirps probe the filter, producing responses whenever the instantaneous chirp frequency correlates with the filter's spectral components. By completing the square on the exponentials in Eq. (9), we verify that Eq. (9) is simply the correlation of $H(2\pi\kappa t)$ with the chirp:

$$\begin{aligned} \langle \rho_{12}(t) \rangle = & \mathcal{D} C \int_{-\infty}^{\infty} d\omega_3 H(\omega_3) \\ & \times \exp\left(\frac{i}{4\pi\kappa} \{\omega_3 + [2\pi\kappa(t + t_0) - \omega_c]\}^2\right) \\ & \times \exp[-i\pi\kappa(t + t_0)^2] \exp[i\omega_c(t + t_0)]. \end{aligned} \quad (10)$$

We rewrite Eq. (10) as a set of convolutions, neglecting the temporal offset, t_0 :

$$\begin{aligned} \langle \rho_{12}(t) \rangle \propto & \{ [H(2\pi\kappa t) * \exp(i\pi\kappa t^2)] \\ & \times \exp(-i\pi\kappa t^2) \} \\ & * \delta(2\pi\kappa t - \omega_c). \end{aligned} \quad (11)$$

If the chirp rate is slow enough, the convolution largely cancels at points in the convolution integral far from the point of stationary phase,²⁷ allowing us to approximate

$$E_o(t) \propto H(2\pi\kappa t) \exp(-i\pi\kappa t^2), \quad (12)$$

where $E_o(t)$ is the output field, and we have ignored the convolution with the chirp start frequency, ω_c . Heterodyne detecting the output field produces a signal proportional to the signal power spectrum as blurred out by a Lorentzian of width $2/T_2$.

4. Convolve–Multiply–Convolve Transforms for Fast Readout

Using slow chirps to interrogate spectral holes allows us to approximate the convolution in Eq. (11) as the direct readout given in Eq. (12). But how slow is slow enough? To resolve a spectral hole of width $\Delta\nu$, the chirp must dwell on the hole for a time equal to or greater than $1/\Delta\nu$, limiting the chirp rate to $\kappa < \Delta\nu$.²⁸ If the chirp rate exceeds this limit, the spectral holes distort the system's response to the chirp. Spectra appear shifted and broadened in time and also exhibit asymmetric, oscillatory behavior.²⁹ To guarantee unity probability of intercept, we must read the entire bandwidth of the SHB crystal before the excited state lifetime elapses. This implies a chirp rate of 2 MHz/ μ s to read the 20 GHz bandwidth of Tm³⁺:YAG in 10 ms. To maintain a resolution of 100 kHz, the slow-chirp limit suggests that the chirp rate cannot exceed 10 kHz/ μ s. Fortunately, we can circumvent the slow-chirp limit to get a broad bandwidth and fine resolution by applying a simple post-processing algorithm to recover the power spectrum from detected signals.³⁰

Because spectral holes act as narrowband filters, they begin oscillating in response to excitation from the chirp as the chirp comes into resonance. As the chirp's instantaneous frequency changes, the chirp beats against the decaying filter oscillation to produce a distorted output.³¹ In this case, the SHB ions, which we characterize as two-level systems, act just like underdamped classical filters. If we know the form of the read chirp, we can recover the recorded power spectrum by convolving the detected intensity with the conjugate of the read chirp^{29,30}:

$$\begin{aligned} H(2\pi\kappa t) &\propto E_o(t) * \exp(-i\pi\kappa t^2) \\ &= [H(2\pi\kappa t) * \exp(i\pi\kappa t^2)] * \exp(-i\pi\kappa t^2) \\ &= \mathcal{F}^{-1}\{\mathcal{F}[H(2\pi\kappa t)] \times \exp[-i\omega^2/(4\pi\kappa)]\} \\ &\quad \times \exp[i\omega^2/(4\pi\kappa)]. \end{aligned} \quad (13)$$

Chang *et al.*³⁰ recently derived this result for SHB processes using the Kramers–Kronig relations. They apply an algorithm suggested by Eq. (13) to both simulations and data from low-bandwidth SHB spectrum analysis experiments performed in sequential write–read fashion with exceptionally clean results.^{15,16} The algorithm is a three-step process: (i) FFT the raw data, (ii) multiply the result by the FFT of the chirp, and (iii) inverse FFT the resulting product. We apply this algorithm in postprocessing to recover a copy of the signal power spectrum whose resolution is limited only by the convolution of the homogeneous linewidth with the read laser linewidth. Because the crystal acts as a linear system when probed with a low-power chirped beam, any signal power spectrum can be recovered as long as we account for saturation during the recording process.³⁰

At first glance, it may appear that we need at least $2\kappa t^2$ points to adequately sample the chirp used for deconvolution. This would defeat the idea of using

low-bandwidth electronics to detect and process the data. Instead, we recognize that the highest frequency we detect is κT_2 , the beat frequency between the chirp and the narrowest spectral hole, which has a width $\Delta\nu = 1/T_2$. When we FFT the detected signal, the result does not have significant frequency components above κT_2 . This means that the product in step (ii) of the recovery algorithm is zero for frequencies higher than a few times κT_2 , so we can neglect the higher frequency components of the chirp. We need only a few times $2\kappa T_2 t$ points to successfully deconvolve the detected intensity.

We can also recognize that the convolution of $H(2\pi\kappa t)$ with a chirp in Eq. (10) corresponds to the Fourier-optics description of image propagation through free space.²⁷ In this context, Eq. (13) is analogous to phase conjugation. We can also apply the remaining two thirds of the convolve–multiply–convolve chirp transform to recover an image of the signal power spectrum, scaled and multiplied by a quadratic phase factor:

$$\begin{aligned} H(-2\pi\kappa t)\exp(i4\pi\kappa t^2) &= \{[H(2\pi\kappa t) * \exp(i\pi\kappa t^2)] \\ &\quad \times \exp(-i2\pi\kappa t^2)\} \\ &\quad * \exp(i\pi\kappa t^2). \end{aligned} \quad (14)$$

This is analogous to single-lens imaging, where $H(2\pi\kappa t)$ is the object and the recovered signal is the image. Multiplying by the conjugate of the phase factor reproduces the scaled object. A two-lens telescope would produce an inverted image of the recorded power spectrum without the additional phase factor. In contrast, the multiply–convolve–multiply chirp transform algorithm used by the chirp-transform spectrum analyzer described in Section 2 corresponds to performing a Fourier transform with a single lens.

5. Saturation Behavior and Dynamic Range

Perturbation models of interactions between signal and chirp beams in SHB media provide insight into the resolution and bandwidth performance of SHB spectrum analyzers, but they do not address limits on dynamic range and resolution due to saturation. In third-order perturbation theory, detected fields are linear in signal power, which is exactly what heuristic models suggest. Two-level systems, however, saturate both coherently and incoherently once incident radiation grows too strong. Illuminating two-level systems with a cw signal beam excites resonant absorbers from the ground state to the excited state, leading to a change in steady-state absorption at the illumination frequency—the spectral hole. At low power levels, spectral hole depth grows linearly with incident power spectral density. Hole depth continues to grow linearly until the medium starts to saturate, at which point hole depth starts to grow sublinearly. Hole depth stops changing once the crystal becomes completely saturated, but the hole broadens at high signal power as the signal excites slightly off-resonant ions.

We explain the amplitude performance of SHB spectrum analyzers by looking at two processes in sequence: (i) spectral hole creation by a signal beam and (ii) spectral hole interrogation by a chirped readout beam. We find the spectral hole depth by integrating through the propagation- and frequency-dependent absorption, $\alpha(z, \omega)$. As the signal beam propagates through the crystal, it is absorbed, decreasing the power available for writing the spectral hole, so the spectral hole becomes progressively shallower with propagation distance.

Even though hole depth varies as a function of propagation distance, we can only measure the hole depth as integrated over the entire crystal thickness by the read beam. The read beam probes the hole depth through the length of the crystal, so the transmitted readout intensity increases as the hole gets deeper. The dynamics of hole depth variation with propagation distance explain the different amplitude performance regimes and dynamic range of integrating SHB spectrum analyzers.

A. Spectral Hole Growth

In steady state, we can use the wave equation to write an expression for the complex absorption that depends on the strength of the incident beam:

$$\alpha(z) = -i \frac{k}{2\epsilon} \frac{\mathcal{P}(z)}{\mathcal{E}(z)}, \quad (15)$$

where $\mathcal{E}(z)$ and $\mathcal{P}(z)$ are the slowly varying amplitude envelopes of the incident field, $E(z, t)$, and the macroscopic polarization, $P(z, t)$, respectively; k is the wave vector; and ϵ is the material permittivity. The intensity of the incident field evolves as

$$\frac{dI(z)}{dz} = -2 \operatorname{Re}\{\alpha(z, \omega)\}I(z), \quad (16)$$

where $I(z) = (c\epsilon/2) |\mathcal{E}(z)|^2$, and c is the speed of light. Numerical integration of these equations yields the aggregate absorption as a function of signal intensity. Before integrating, however, we must derive an expression for $\mathcal{P}(z)$ in terms of the incident field.

We begin our derivation of $\mathcal{P}(z)$ by writing the equations of motion for a two-level system exposed to a signal field $E(z, t)$ after Meystre and Sargent²⁵:

$$\dot{w}(z, \omega, t) = -\frac{w(z, \omega, t) - w_{\text{eq}}}{T_1} + i \frac{\mu_{12}}{\hbar} [\rho_{21}(z, \omega, t)E(z, t) - \text{c.c.}], \quad (17)$$

$$\dot{\rho}_{12}(z, \omega, t) = -\left(i\omega + \frac{1}{T_2}\right)\rho_{12}(z, \omega, t) - i \frac{\mu_{12}}{2\hbar} E(z, t)w(z, \omega, t), \quad (18)$$

where the dots indicate time derivatives and

$w(z, \omega, t) = \rho_{22}(z, \omega, t) - \rho_{11}(z, \omega, t)$ is the population inversion between the excited and the ground states, which are themselves functions of depth (z), frequency (ω), and slow time (t). Distributing the population evenly between the ground and the excited states [$w(z, \omega, t) = 0$] renders the medium transparent, and inverting the population [$0 < w(z, \omega, t) \leq 1$] introduces gain.

Initially, all the absorbers are in the ground state, so the equilibrium inversion is $w_{\text{eq}} = -1$. In inhomogeneously broadened media, the absorbers are distributed across an inhomogeneous band given by

$$\mathcal{G}(\omega) = \frac{1}{\Delta\omega\sqrt{\pi}} \exp\left[-\left(\frac{\omega}{\Delta\omega}\right)^2\right], \quad (19)$$

where the $1/e^2$ width is $\Delta\omega = 2\pi/T_2^*$. $\mathcal{G}(\omega)$ is normalized to unit area.

In spectrum analysis, we illuminate the crystal with two beams: the signal beam and the chirped read beam. In this analysis, we assume that the chirp beam changes frequency slowly on the scale of the interaction, so we express it as a cw excitation. For a signal consisting of single cw tone, the total field is

$$E(z, t) = \mathcal{E}_s(z)\exp[i(\omega_s t - k_s z)] + \mathcal{E}_r(z)\exp[i(\omega_r t - k_r z)], \quad (20)$$

where $\omega_{s,r}$ are the signal and read frequencies and $k_{s,r}$ are the signal and read wave vectors. At steady state, $\dot{w}(z, \omega, t) = 0$, so we integrate Eq. (18) to solve for the off-diagonal matrix element $\rho_{12}(z, \omega, t)$:

$$\rho_{12}(z, \omega, t) = -i \frac{\mu_{12}}{\hbar} w(z, \omega, t) \times \{\mathcal{E}_s(z)\exp[i(\omega_s t - k_s z)]\gamma(\omega - \omega_s) + \mathcal{E}_r(z)\exp[i(\omega_r t - k_r z)]\gamma(\omega - \omega_r)\}, \quad (21)$$

where $\gamma(\omega - \omega_{s,r})$ is a complex Lorentzian given by

$$\gamma(\omega - \omega_{s,r}) = \frac{1}{(1/T_2) - i(\omega - \omega_{s,r})}.$$

The complex Lorentzian accounts for dispersion and attenuation of the incident fields.

Next we solve for the population inversion. We assume that the read beam is weak, so we neglect its contributions (coherent or incoherent) to the population inversion. At steady state, the population inversion depends only on the intensity of the signal beam,

$$w(z, \omega, t) = \frac{\mathcal{G}(\omega)w_{\text{eq}}}{1 + [I_s(z)/I_{\text{sat}}]\mathcal{L}(\omega - \omega_s)}, \quad (22)$$

where $I_{\text{sat}} = (c\epsilon/2) |\hbar/\mu_{12}|^2/(T_1 T_2)$ is the saturation intensity and $\mathcal{L}(\omega - \omega_r)$ is a real Lorentzian given by

$$\mathcal{L}(\omega - \omega_0) = \frac{(1/T_2)^2}{(1/T_2)^2 + (\omega - \omega_0)^2}.$$

For large values of I_s , the inversion asymptotically approaches 0, indicating that the medium becomes transparent at the signal frequency at high signal intensities. The real Lorentzian and the saturation intensity determine the width of the spectral hole.

We define the macroscopic polarization as $P(z, t) = 2\mu_{12}\rho_{12}(z, \omega, t)$. Using this definition in conjunction with the derivation of Eq. (15) from the wave equation allows us to break the absorption into a component at the signal frequency and a component at the read frequency:

$$\alpha(z) = \alpha_s(z) + \alpha_r(z). \quad (23)$$

By matching exponentials when using the macroscopic polarization to derive Eq. (15), we can substitute that part of Eq. (22) that is dependent on the signal beam into Eq. (21) and use our expression for the polarization to solve for the frequency-dependent absorption for the signal beam:

$$\alpha_s(z, \omega) = \frac{\alpha_0}{T_2} \frac{\mathcal{G}(\omega)\gamma(\omega - \omega_s)}{1 + [I_s(z)/I_{\text{sat}}]\mathcal{L}(\omega - \omega_s)}, \quad (24)$$

where $\alpha_0 = -(k\mu_{12}^2 NT_2)/(2\epsilon\hbar)$ is the small-signal absorption coefficient and N is the total number of absorbers. The change in absorption at the signal frequency, $\Delta\alpha_s(z)$, is the spectral hole. At $I_s = I_{\text{sat}}$, $\alpha_s(z, \omega_s, t)$ falls to half of its nominal value, hence the term saturation intensity.

Figure 2 shows the spectral hole depth as a function of detuning from the signal laser frequency, ω_s , and propagation distance for several values of input intensity $I_s(z = 0)$. For small values of $I_s(0)$, the spectral hole remains shallow, as shown in Fig. 2(a). Spectral hole depth grows with increasing $I_s(0)$ until $I_s(0) = I_{\text{sat}}$, at which point the front edge of the crystal begins to saturate with $\Delta\alpha(z, \omega_s) = 0.5$, as shown in Fig. 2(b). Increasing intensity further saturates the front of the crystal, while the back of the crystal continues to record changes in the spectral hole depth, as shown in Fig. 2(c). Eventually, the crystal becomes saturated front to back, as shown in Fig. 2(d). Further increasing the intensity causes the spectral hole to grow wider rather than deeper, a phenomenon known as power broadening.²⁶ Figures 2(c) and 2(d) both show the onset of power broadening.

B. Spectral Hole Interrogation

To interrogate the spectral holes, we illuminate the SHB crystal with a pair of chirped beams of intensity $I_r(0)$, as shown in Fig. 1. The read beam probes the spot illuminated by the signal beam, and the background beam probes a different spot to measure the crystal's background absorption. We match exponentials for the read beam in Eqs. (21) and (23) to write the absorption at the read frequency:

$$\alpha_r(z; \omega_r, \omega_s) = \frac{\alpha_0}{T_2} \int_{-\infty}^{\infty} \frac{\mathcal{G}(\omega)\gamma(\omega - \omega_r)}{1 + [I_s(z)/I_{\text{sat}}]\mathcal{L}(\omega - \omega_s)} d\omega. \quad (25)$$

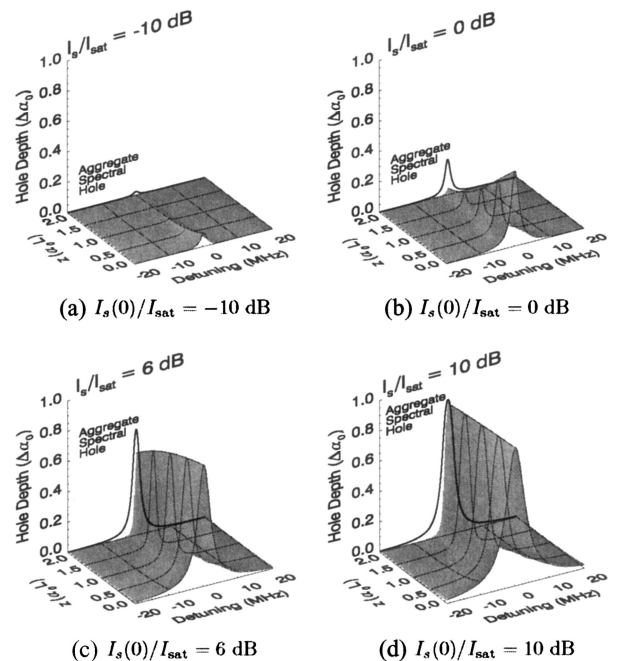


Fig. 2. Absorption variation with frequency detuning for different values of $I_s(z = 0)$. The dark line at $z = 2\alpha_0 L$ is the absorption integrated over the propagation distance. As intensity increases, the hole begins to saturate and broaden. The saturation point moves from the input to the output of the crystal until the crystal is completely saturated.

This is the interaction of the read beam, as represented by a complex Lorentzian centered at ω_r , with the spectral hole, as represented by a real Lorentzian centered at ω_s . When the read frequency equals the signal frequency, the absorption is

$$\alpha_r(z; \omega_r = \omega_s) = \frac{\alpha_0}{T_2} \frac{\mathcal{G}(\omega_r)}{\sqrt{1 + [I_s(z)/I_{\text{sat}}]}}. \quad (26)$$

Here, we assume that the inhomogeneous band is much broader than either of the Lorentzians in Eq. (25), so we sample the inhomogeneous weighting at the read frequency and pull it out of the integral.

We detect the read and background beams on a differential detector to produce a differential current,

$$i_d(L; \omega_r, \omega_s) = \text{Re} \left\{ \exp \left[\int_0^L -2\alpha_r(z; \omega_r, \omega_s) dz \right] - \exp \left[-2 \frac{\alpha_0}{T_2} \mathcal{G}(\omega_r) L \right] \right\} \mathcal{R} I_r(0) A, \quad (27)$$

where L is the crystal thickness, \mathcal{R} is the detector responsivity, and A is the beam overlap area. In an angled-beam geometry, such as that shown in Fig. 1, the read beam does not overlap completely in space with the spectral hole, requiring a full integration across the read beam's Gaussian profile. Switching to a counterpropagating beam geometry would allow the read beam to illuminate the entire volume containing the spectral hole. For simplicity, we ignore

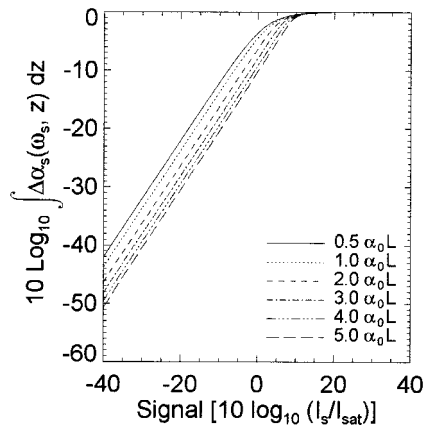


Fig. 3. Spectral hole depth at the signal beam frequency as a function of signal beam intensity.

the transverse beam profile and overlap in this analysis.

At small signal levels, aggregate spectral hole depth grows linearly with signal intensity, as shown in Fig. 3, and differentially detected current varies linearly, as shown in Fig. 4(a). As signal intensity increases, the spectral hole begins to saturate, rendering the crystal nearly transparent at the signal frequency. This causes the detected current to grow exponentially with signal intensity for thicker crystals, as shown in Fig. 4(b). At even higher signal intensity, the hole becomes fully saturated, leaving the crystal fully transparent at the signal frequency. The current also reaches its saturation value at this point.

Once the crystal begins to saturate, the spectral hole becomes broader as the signal beam partially excites off-resonant absorbers.²⁶ Power broadening degrades resolution and limits sensitivity in adjacent spectral bins. We determine the spectral hole's FWHM by integrating $\alpha(z)$ over different optical thicknesses and fitting to the FWHM of the aggregate holes. Figure 5 shows the logarithm of the FWHM, scaled by the homogeneous linewidth, as a function of signal intensity. The FWHM remains constant at the homogeneous linewidth until saturation begins, at which point the aggregate spectral hole width starts to grow as the square root of signal intensity, as shown in Fig. 5.

Squaring the FWHM and multiplying the result by the differentially detected current yields a figure of merit we call peak volume. This approach is based on a similar figure of merit suggested by Babbitt and Mohan.³² They measured the detected power by looking at peak area, the product of the detected signal with the detected FWHM. Peak volume grows linearly with signal intensity, as shown in Fig. 6, except for a slightly kinked region during the transition from linear to saturation regimes. Measuring peak volume instead of detected current alone allows us to continue monitoring signal power well past the saturation limit.

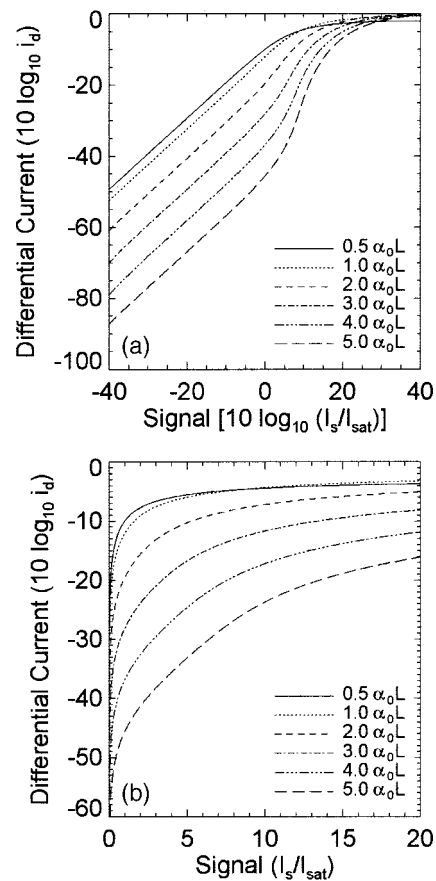


Fig. 4. (a) Log-log and (b) log-linear plots of differentially detected current i_d as a function of input signal intensity $I_s(0)$ for several values of $\alpha_0 L$. Differential current is normalized to $\mathcal{R}I_r(0)A$. Variation is linear until the crystal begins to saturate, at which point variation becomes exponential for thick crystals until total saturation occurs.

C. Additional Broadening Mechanisms

There are, of course, other mechanisms that increase the homogeneous linewidth. At high temperature, direct and Raman phonon processes contribute significantly to the homogeneous linewidth, reducing the resolution of our system. At 4.8 K, the homogeneous linewidth is about 100 kHz, but at 6 K, the homogeneous linewidth increases to 1 MHz.⁷ Because thermal broadening substantially degrades resolution, we try to keep the crystal as cold as possible when writing and reading the signal power spectra.

Excitation-induced frequency shifting can also reduce the resolution.³³⁻³⁵ This effect, also known as instantaneous spectral diffusion,³⁶ occurs when incident radiation excites ions, inducing electric dipole moments in a subset of the ionic population. The interaction between dipole moments shifts the resonance frequencies of the neighboring ions by changing the local fields. Increasing either the signal bandwidth or the excitation strength per unit of bandwidth increases the strength of this effect because the probability of exciting nearby ions goes up.³⁷ Recording a broadband chirp (just as we do in

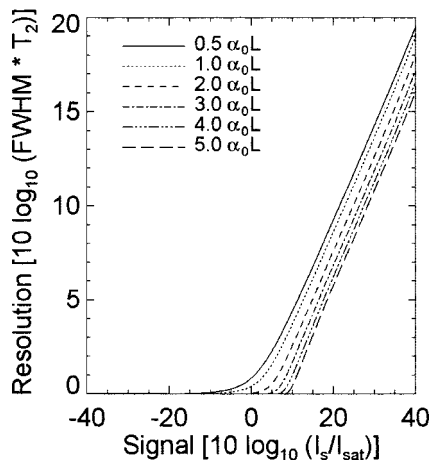


Fig. 5. Logarithm of the detected spectral hole FWHM normalized to homogeneous linewidth $1/T_2$ as a function of input signal intensity $I_s(0)$. The hole width remains constant at $1/T_2$ until saturation begins, at which point the hole width starts to grow as the square root of signal beam intensity.

our experiment) should produce the full effects of excitation-induced frequency shifting.

Dynamic fluctuations in the ions' local environment also increase the homogeneous linewidth. This broadening mechanism, called spectral diffusion, has been attributed to electric and magnetic dipole spin-flip interactions.³⁸ Each ion's resonance frequency undergoes an irreversible random walk as the local spin configuration changes, producing a hole whose width increases in time by as much as an order of magnitude.³⁹ This broadening mechanism should reach its equilibrium state for cw or multitone holes that are burned continuously (such as the square wave we record in our experiment). Our experimental results are almost certainly affected by both excitation-induced frequency shifting and spectral diffusion. In some cases, we may be able to improve the resolution by decreasing the burning time or readout latency.

6. Extending Dynamic Range

Spectrum analyzers operate with either large dynamic range or good sensitivity, but not both simultaneously. Good sensitivity typically requires amplifying the input signal; amplification introduces spurious intermodulation products that place upper limits on the signal power.¹ By using peak volume instead of detected current, we can extend the dynamic range of the SHB spectrum analyzer without using an amplifier, avoiding limits imposed by intermodulation products. Of course, using peak volume to determine signal strength comes at the cost of degraded resolution at large signal power.

Instead of trading sensitivity for extended dynamic range, we can use the degenerate information contained in double-sideband optical modulation to increase dynamic range and improve sensitivity simultaneously. Modulating the signal beam with an EOM produces an output with two sidebands cen-

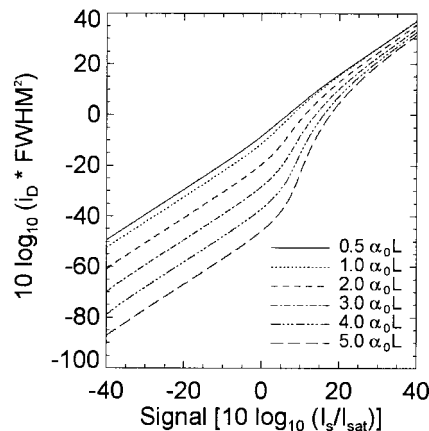


Fig. 6. Peak volume ($\text{FWHM}^2 \times i_d$) as a function of input signal intensity $I_s(0)$.

tered about an optical carrier, as shown at the top of Fig. 7(a). Illuminating a SHB crystal of thickness $\alpha_0L = 5$ with the carrier tuned to the center of the inhomogeneous band produces a set of mirror-image holes. For example, a 6 GHz rf carrier with 2 MHz amplitude modulation will produce symmetric hole triplets as shown in Fig. 7(a). In this case, the optical power in the rf sidebands is $I_s/I_{\text{sat}} = 10$ dB. Close-ups of the upper- and lower-sideband holes, shown at the bottom of Fig. 7(a), reveal that the holes are completely degenerate. We can simply ignore one set of holes, or we could average the two sidebands to get a 3 dB increase in signal-to-noise ratio and dynamic range.

We can also recognize that crystals of different optical thicknesses respond differently to identical signal powers. Figure 4 shows that a signal intensity of 20 dB below the saturation intensity produces a differentially detected current of about -33 dB [as normalized to $\mathcal{R}I_r(0)A$] in a crystal of thickness $\alpha_0L = 1$, and increasing the thickness to $\alpha_0L = 5$ causes the detected current to fall to about -67 dB. Increasing the signal intensity by 30 dB causes the detected currents in each case to increase by 28 and 43 dB to about -5 and -24 dB, respectively. Thinner crystals exhibit greater sensitivity, while thicker crystals saturate at higher signal intensity. Thinner crystals are better for detecting weak signals, and thicker crystals are better for detecting strong signals.

Although α_0L is fixed for a given crystal, the inhomogeneous frequency weighting, $\mathcal{G}(\omega)$, means that different spectral components propagate through different optical thicknesses depending on their detuning from resonance. Tuning the optical carrier away from the line center, as shown in Fig. 7(b), moves one sideband away from resonance and the other sideband toward resonance. In this example, the lower sideband experiences smaller optical thickness and is therefore more sensitive. The upper sideband experiences greater optical thickness and therefore saturates at higher power, as shown in the bottom of Fig. 7(b). We use the same modulation parameters as in Fig. 7(a): a 6 GHz rf carrier with 2 MHz amplitude

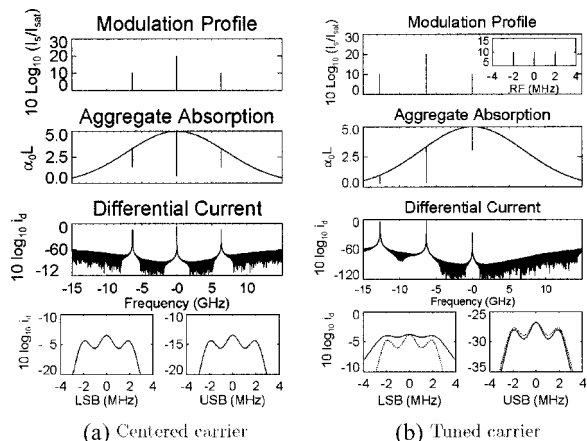


Fig. 7. Input spectra, aggregate spectral hole depth, and differentially detected current for double-sideband modulation with resonant and tuned optical carriers. The sidebands (inset, top) are three rf tones centered at about 6 GHz and spread over 4 MHz, with power equivalent to $I_s(0)/I_{\text{sat}} = 10$ dB. Close-ups (bottom) of the differentially detected sidebands show resolution.

modulation, with optical power in the sidebands of $I_s/I_{\text{sat}} = 10$ dB. The close-ups at the bottom of Fig. 7(b) show the two sidebands (solid curves) and overlaid versions of the untuned sidebands (dotted curves). The lower sideband has already begun to saturate, as shown by the decreased resolution. The upper sideband resolution is still at the homogeneous linewidth limit. The optical thicknesses experienced by the sidebands of a broadband spectrum vary continuously, as do the sensitivity and dynamic range trade-offs at different frequencies, so the behavior at each frequency offset for both sidebands needs to be carefully calibrated.

7. Experimental Demonstration of a Spectral-Hole-Burning Spectrum Analyzer

We perform spectrum analysis in a 0.1% Tm^{3+} :YAG crystal with a thickness of approximately $2\alpha_0 L = 1.1$, as shown in Fig. 8. Illuminating Tm^{3+} :YAG with laser light at 793.3 nm excites the ${}^3\text{H}_6$ to ${}^3\text{H}_4$ transition in Tm^{3+} , which has an inhomogeneous linewidth of about 20 GHz. The excited state, which has a lifetime of hundreds of microseconds, decays preferentially to the ${}^3\text{F}_4$ level, which has a lifetime of about 10 ms and acts as a bottleneck state.⁴⁰ Although Tm^{3+} :YAG is a three-level system, its absorption as measured by the chirp beam is primarily a function of the ground-state population. Even though the excited state has a short lifetime, it decays to a bottleneck state, so the change in absorption persists until the bottleneck lifetime elapses and the excited ions decay all the way back down to the ground state. This allows us to model Tm^{3+} as a two-level system.

We use a pair of external-cavity diode lasers (ECDLs) to generate the cw and chirp beams that act as signal and read beams, respectively. We use ECDLs because they are easy to tune over many gigahertz of bandwidth and are available at a wavelength of 793.3 nm. The cw output of the first ECDL, the signal laser, propagates into a variable-ratio, polarization-maintaining (PM) fiber coupler that splits 5% of the input power into a stabilization beam (discussed below) and the remaining 95% of the input power, about 3 mW, into a signal beam. An intensity EOM modulates the signal beam with upper and lower sidebands of a rf signal before the beam is focused by a 300 mm focal-length lens to a 150 μm spot inside the crystal. We bias the EOM at its transmission null to prevent the carrier from saturating the crystal and obscuring

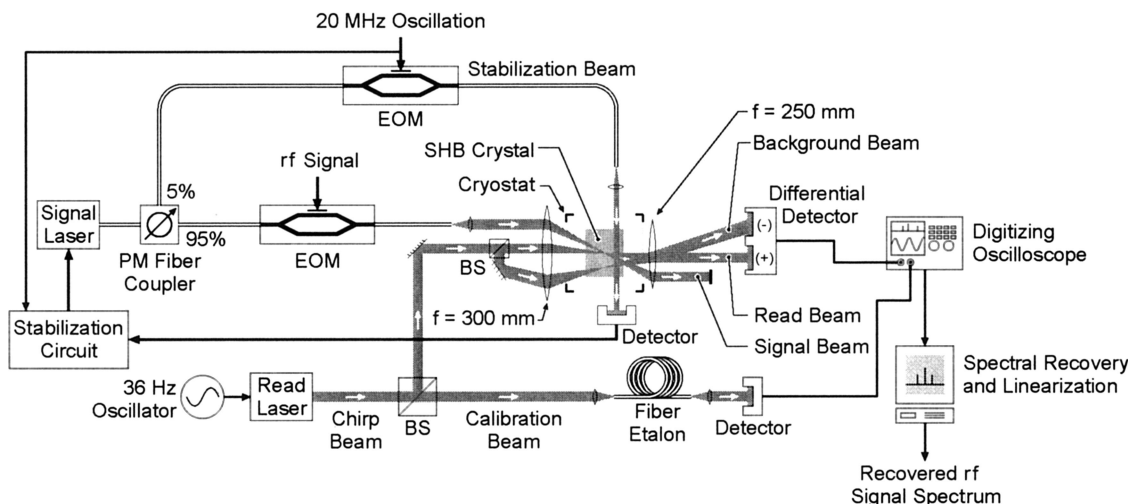


Fig. 8. High bandwidth spectrum analyzer based on SHB. A PM fiber coupler splits the signal laser beam into a signal beam and a stabilization beam, which locks the laser to a spectral feature in the crystal. The signal beam writes the signal spectrum into the SHB crystal. A 36 Hz oscillator drives the read laser to produce a chirp beam, which is split into a read beam, a background beam, and a calibration beam by a pair of beam splitters (BSs). The read and background beams probe the crystal to produce a temporal map of the rf signal spectrum. The calibration beam passes through a fiber etalon to produce a measurement of the chirp beam's frequency nonuniformity. Postprocessing oscilloscope data using spectral linearization and recovery techniques yields the signal power spectrum.

adjacent spectral bins. Null bias is quadratic in intensity modulation but linear in field modulation, making it the best operating point for the field detection operation performed by SHB crystals. The signal beam exits the crystal, is recollimated, and is blocked by a razor blade.

We generate the chirp beam by tuning the angle of the external mirror in the second ECDL with a piezoelectric transducer. Changing the grating angle shifts the frequency of the output beam, and linear changes produce chirps. We would like to use a sawtooth voltage to generate a series of linear chirps, but piezoelectric transducers respond poorly to sharp changes in drive voltage, so we use a 36 Hz sine wave instead. Using a sinusoidal drive signal provides a linear response over the desired frequency range without inducing higher harmonics in the transducer. Increasing the drive frequency to 100 Hz would sweep the chirp across the crystal bandwidth twice (once up and once down) every time the excited state lifetime elapses.

The present drive signal sweeps the chirp beam back and forth in frequency over the crystal's inhomogeneous bandwidth at a rate of about 14 MHz/ μ s, well beyond the Fourier-limited chirp rate of 1 MHz/ μ s. We use a pair of beam splitters to split the chirp beam into a read beam and a background beam, each with a power of 150 μ W, and a spectral calibration beam with a power of about 2 mW. The read beam propagates parallel to the signal beam, as shown in Fig. 8, before being focused to the same 150 μ m spot in the crystal illuminated by the signal beam. The read beam then propagates out of the crystal, is recollimated, and strikes the (+) port of an 80 MHz differential detector. As the read beam sweeps in frequency, the detector senses dips in the transmitted intensity corresponding to the spectral holes burned into the crystal's absorption profile by the signal beam.

The read beam also probes the crystal's background absorption profile, which is constant throughout the crystal but varies with frequency. We measure background absorption with the background beam and subtract it from the read beam with the differential detector described above to give a zero-background measured voltage. Because the background beam propagates at an angle with respect to the signal and read beams, it is focused to a different 150 μ m spot in the crystal. It exits the crystal, is recollimated, and strikes the (-) port of the differential detector, which emits the measured signal after background subtraction.

Differential detection eliminates constant background data from the crystal's inhomogeneous absorption profile, but it cannot compensate for frequency distortion due to frequency jitter in the lasers. Therefore we stabilize the signal laser, described in Subsection 7.A, but not the read laser. Stabilizing the read laser would require a reference capable of chirping across >20 GHz of bandwidth in under 10 ms or the use of interferometric chirp detection and correction.^{41,42} Instead, we use a calibration beam to mea-

sure nonuniformities in the chirp rate as part of a chirp calibration system, which we describe in Subsection 7.B.

We use a 1 GHz, 4 Gsample/s digitizing oscilloscope with >6 effective bits of resolution to capture the output from the differential detector. As the read laser's frequency tunes across the crystal's absorption band, the differential detector records spectral holes burned by the signal beam as changes in detected intensity. Because we do not stabilize the read laser, the chirp beam jitters in frequency on a shot-to-shot basis, so we have to collect data in single shots. We use the spectral hole generated by the dc peak from the optical carrier as a peak trigger for each trace collected by the oscilloscope. The dc peak also serves as an absolute frequency reference when mapping the detector output to the spectral domain of the signal. We apply a spectral linearization algorithm²¹ to correct for chirp nonuniformity before using the spectral recovery algorithm³⁰ to remove ringing induced by fast readout. We scale the amplitude of the captured signal using the curves shown in Fig. 4 to produce the signal power spectrum.

A. Signal Laser Stabilization

If the signal laser jitters in frequency during the writing process, then the crystal records a blurry copy of the rf signal spectrum. To prevent this loss of resolution, we use the stabilization beam to lock the signal laser to a spectral feature in an isolated spot in the SHB crystal,⁴³ as shown in Fig. 8. The stabilization beam propagates through a second EOM, which is driven by a 20 MHz oscillation, travels through the crystal, and finally illuminates a low-bandwidth detector. A mixer beats the detector output against the 20 MHz oscillation to produce a dc feedback signal that drives current and piezoelectric servos to control the frequency of the signal laser.^{44,45}

When first turned on, the signal laser jitters in frequency, so the stabilization beam burns a wide spectral hole into the crystal's absorption profile. A low-bandwidth detector measures the frequency-domain distortion that the spectral hole induces in the transmitted signal. A mixer beats the detected change in the transmitted signal against another copy of the oscillation driving the EOM, producing a low-frequency heterodyne beat. The beat term controls current and piezoelectric servos. The piezoelectric servo controls slow fluctuations by moving the grating that determines the length of the laser's external cavity, and the current servo controls fast fluctuations by changing the diode current to rapidly tune the laser.

The signal laser continues to burn a hole in the crystal's absorption profile, but the hole becomes narrower as the laser frequency stabilizes and the wings of the initial features decay to the ground state. Eventually, the hole narrows to the homogeneous linewidth, and the laser stabilizes to a fraction of the homogeneous linewidth.⁴³ The present write laser has a stabilized linewidth of about 10 kHz, while the unstabilized laser linewidth is 1 MHz.

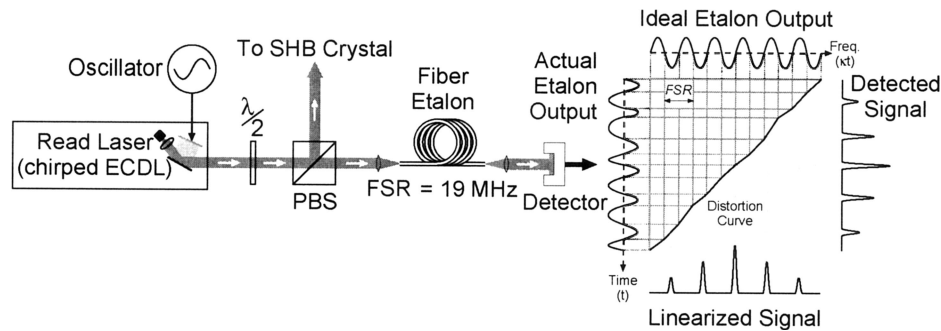


Fig. 9. Spectral linearization. A half-wave plate ($\lambda/2$) used with a polarizing beam splitter (PBS) sends part of the read laser's output through a fiber etalon, which has a free spectral range of about 19 MHz. The oscillator chirps the read laser, causing the etalon output to fluctuate in intensity. The algorithm compares the actual etalon output to the ideal etalon output, generating a map of the chirp distortion for use in linearizing the raw data.

B. Spectral Linearization

Stabilizing chirped lasers is much more difficult, primarily because, to the best of our knowledge, electronic chirped references that are both fast and broadband do not exist. If they did, we could drive another EOM with the reference to produce the chirp beam required to read the spectrum. However, using such electronic chirp sources eliminates some of the advantages of spectrum analysis using all-optical techniques. There are a variety of optical techniques capable of producing broadband chirps, most of which involve tuning ECDLs or fiber lasers by heating them or by moving their components with piezoelectric devices. Temperature tuning is too slow to be useful for our application, and piezoelectric tuning suffers from noise and stiction, both of which produce unique nonuniformities in the laser chirp. Rather than attempt to actively correct the nonuniformities in a piezoelectrically tuned laser chirp,⁴¹ we record them so that we can compensate for them in postprocessing.²¹

Ideally, the chirp beam should sweep linearly in frequency. However, because the piezoelectric device used to tune the output frequency of the read laser does not always respond linearly or deterministically to the applied voltage, the read laser output sweeps nonuniformly in frequency. Accurate measurement of the chirp rate nonuniformity requires detecting the chirp using interferometry,⁴¹ scanning etalons,⁴⁶ or self-heterodyne techniques.⁴² We choose to measure nonuniformity in the chirp rate by transmitting the calibration beam through an etalon composed of a piece of single-mode PM fiber roughly 5.5 m long, which has a free spectral range (FSR) of about 19 MHz. The 4% reflections off the end faces of the fiber are sufficient to produce a sinelike output signal, which we detect during readout using a low-bandwidth detector, as shown in Fig. 9.

Transmitting perfectly linear chirps through etalons produces perfectly periodic outputs, with successive peaks separated in frequency by the etalon's FSR. The chirp rate of the transmitted beam is simply the FSR divided by the sinusoid's period. Transmitting distorted chirps through etalons yields outputs that are no longer perfectly periodic. The peaks still cor-

respond to frequency separations given by the etalon's FSR, but peak separation varies in time as the chirp rate increases or decreases during the chirp's evolution. We do not care about the change in time between spectral holes—we just want to know their separation in frequency. Signals transmitted by the fiber etalon provide the information necessary to match a given moment in time to the corresponding instantaneous chirp frequency, as shown in Fig. 9. We compare detected etalon outputs in the time domain to the ideal etalon output to create a distortion curve. We use the distortion curve to map detected signals from the time domain to the spectral domain. The distortion curve is a map of the instantaneous chirp frequency versus time, so the mapped or linearized signal lies along a spectral abscissa free from nonuniformity.

8. Results and Discussion

Figure 10 shows the raw spectrum of a 420 MHz square wave and a 10–20 GHz, 10 ms long chirp as captured by the digitizing oscilloscope. We use a 1×2 power combiner to drive the EOM with both signals simultaneously. After acquiring the data, we apply linearization and recovery algorithms in sequence. Figure 11 shows experimental data used to map the detected signal from the time domain (t) to the spectral domain (κt). The distortion curve shown in Fig. 11 isn't fine enough to show the nonuniformity in the chirp rate, so we plot the difference between ideal and actual chirp rates in Fig. 12. The nonuniformity

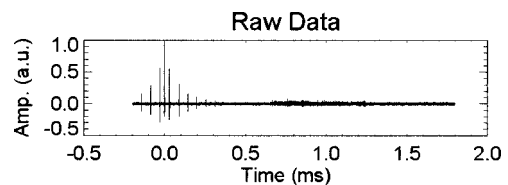


Fig. 10. Raw spectrum of a 420 MHz square wave and a 10–20 GHz chirp as recorded by the SHB crystal and captured on the oscilloscope. The dc peak associated with the optical carrier triggers the oscilloscope and also acts as the zero frequency reference for the linearization and mapping processes.

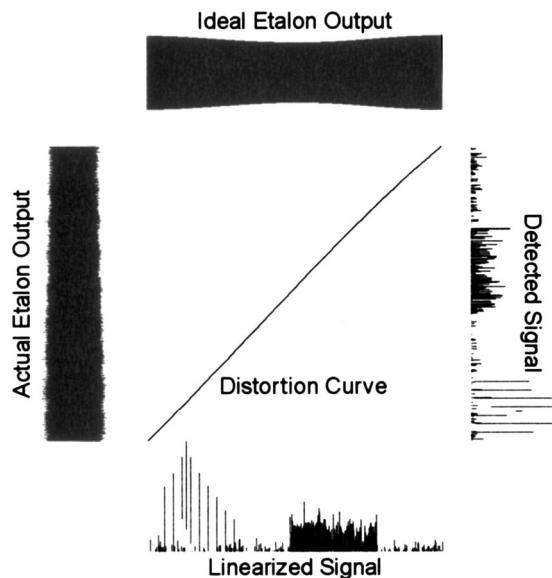


Fig. 11. Spectral linearization algorithm for the experimental data. We show linearized raw etalon output data as the ideal etalon output.

never exceeds $1 \text{ kHz}/\mu\text{s}$, indicating that the chirp is fairly linear.

We test our linearization algorithm using two different methods. First, we apply the algorithm to the actual etalon output itself. The actual etalon output is aperiodic, so its FFT is fairly broad, as shown in Fig. 13(a). Linearizing the etalon output produces a periodic output whose FFT is about 100 times narrower, as shown in Fig. 13(b), indicating that the linearization algorithm corrected for aperiodicity introduced by the nonuniform chirp. Increasing the length of the fiber etalon would decrease the FSR, further improving frequency accuracy. Side peaks 20 dB below the main peak could be an indication we need to use a warping algorithm more sophisticated than linear interpolation.

We also compare the positions of the square-wave harmonics to their expected positions before and after linearization, as shown in Fig. 14. Peaks in the raw data differ from their expected positions with a standard deviation of about 30 MHz across a span of about 8 GHz. After linearization, the standard deviation of this difference falls to about 0.3 MHz, a factor of 100 improvement. Differences in peak location fall

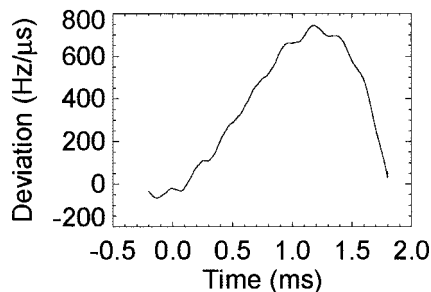


Fig. 12. Difference between ideal and actual chirp rates.

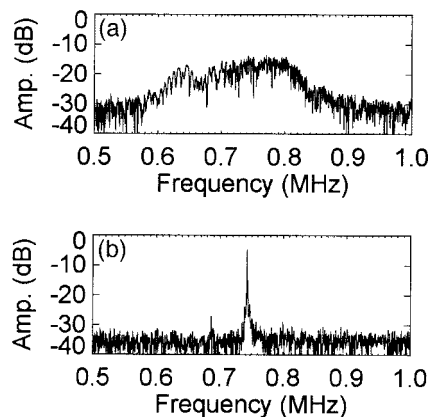


Fig. 13. Spectrum of the reference etalon output (a) before and (b) after spectral linearization.

below the resolution of the current result, demonstrating the effectiveness of the linearization algorithm.

Once the data are linearized, we apply the spectral recovery algorithm. The first-order square-wave peak at 420 MHz shown in Fig. 15(a) exhibits the characteristic oscillations induced by fast chirps. The recovered peak shown in Fig. 15(b) has a FWHM of about 1 MHz and does not exhibit the wild oscillations shown in the raw data. This resolution is about ten times the fundamental limit imposed by the SHB crystal's inhomogeneous linewidth. In our current experiment, the linewidth of the read laser acts as the resolution limit. Switching from chirped ECDLs to chirped fiber lasers, which are commercially available with linewidths of about 3 kHz, could improve resolution.

Figure 16 shows the linearized, recovered, and scaled spectrum of a 420 MHz square wave and a 10–20 GHz chirp. We use the chirp rate and the dc peak of the optical carrier to scale and center the frequency axis. Inspection of the sidebands in the raw data show we are operating in the linear hole depth regime, so we scale the results using the plot shown in Fig. 4 to produce a plot of the relative power spectrum. We plot the power spectrum in Fig. 16. Our measurements compare well to peak heights for ideal

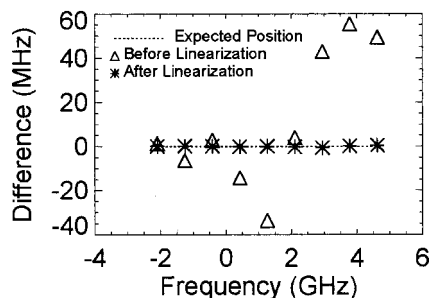


Fig. 14. Error in the positions of the 420 MHz square wave peaks. The error is the difference between the ideal and the actual peak positions, before and after linearization. The standard deviation of the difference drops from 30 MHz before linearization to 0.3 MHz after linearization.

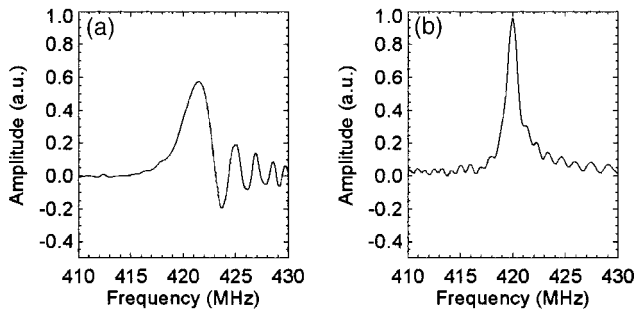


Fig. 15. First-order peak of the 420 MHz square wave (a) without and (b) with spectral recovery (Ref. 30). Ringing present in the unrecovered signal is removed by deconvolving (i.e., by Fourier transforming the raw signal, multiplying the conjugate of the chirp, and Fourier transforming the result) the raw signal from the read chirp to produce the recovered peak. Spectral recovery reduces the FWHM from about 2.5 MHz to 1 MHz.

square waves and to data from a conventional spectrum analyzer.

Unlike conventional spectrum analyzers, which have to operate in a sample-and-hold mode for several seconds to capture the entire chirp, our spectrum analyzer captures and incoherently integrates the spectrum of incident signals in $T_1 = 10$ ms, the excited state time of the SHB crystal. The excited state lifetime of the crystal also determines the maximum duration of the chirp we use to interrogate the altered spectrum of the crystal. We sweep the chirp beam at a rate of about 14 MHz/ μ s, or roughly 14 times the maximum chirp rate as determined by the conventional Fourier limit for a resolution of 1 MHz.

Because the rf sweeper takes 10 ms to sweep from 10 to 20 GHz and waits several milliseconds between chirps, our spectrum analyzer can miss a portion of the signal chirp unless its readout sequence is synchronized to the rf sweeper's output, as shown in Fig. 16. Our spectrum analyzer is actually faster than the rf sweeper, so it captures only a portion of the sweeper's output.

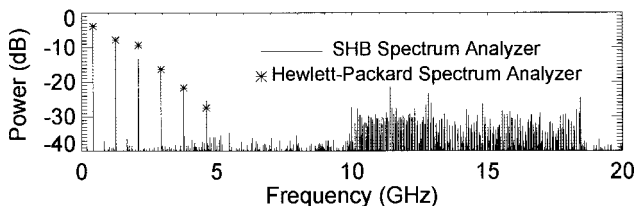


Fig. 16. Relative power spectrum of a 10–20 GHz chirp and a 420 MHz square wave as measured by our SHB spectrum analyzer after linearization and spectral recovery (Ref. 30). The time-bandwidth product exceeds 20,000. We used a digital frequency synthesizer to produce the 10–20 GHz chirp, hence its discretized structure. Because the sweep and readout times are each 10 ms and the sweep and readout are not synchronized, the spectrum analyzer misses the last portion of the chirp.

9. Conclusions

We have demonstrated 20 GHz spectrum analysis with a 40 dB dynamic range and a time-bandwidth product of about 20,000 using a single spot in a Tm³⁺:YAG crystal. Our method of rf spectrum analysis guarantees unity probability of intercept, making it ideal for applications such as channelizing data from broadband rf surveillance systems.

In addition, we can perform spectrum analysis on multiple channels simultaneously in the same crystal, making this approach amenable to processing data from phased arrays.^{47–50} Each channel requires a single optical spot, so a modestly sized crystal could process hundreds of channels in parallel. We believe that the low power requirements and multichannel capability more than offset the need for cryogenic cooling for applications requiring high performance.

We gratefully acknowledge the support of Stephen Pappert through the DARPA Analog Optical Signal Processing program. We also thank Alan Mickelson and John Hauser of CU, Wm. Randall Babbitt of Montana State University, and Kris Merkel of SciMat, Incorporated, for several helpful conversations. M. Colice also acknowledges support from the NSF Integrative Graduate Education and Research Traineeship Optical Science and Engineering Program.

References

1. M. Engelson, *Modern Spectrum Analyzer Theory and Applications* (Artech House, 1984).
2. *Spectrum Analysis Basics*, Application Note 150 (Agilent, 2004), www.agilent.com.
3. *Fundamentals of Real-Time Spectrum Analysis*, Primer, Tektronix (2004), www.tektronix.com.
4. J. L. Anderson, H. B. Brown, and B. V. Markevitch, "Wideband real-time Fourier analyzer using folded spectrum techniques," in *Real-Time Signal Processing II*, T. F. Tao, ed., Proc. SPIE **180**, 146–152 (1979).
5. T. Turpin, "Spectrum analysis using optical processing," Proc. IEEE **69**, 80–92 (1981).
6. Y. Sun, C. W. Thiel, R. L. Cone, R. W. Equall, and R. L. Hutcheson, "Recent progress in developing new rare-earth materials for hole burning and coherent transient applications," J. Lumin. **98**, 281–287 (2002).
7. R. M. Macfarlane, "Direct process thermal line broadening in Tm:YAG," J. Lumin. **85**, 181–186 (2000).
8. T. W. Mossberg, "Time-domain frequency-selective optical data storage," Opt. Lett. **7**, 77–79 (1982).
9. Y. S. Bai, W. R. Babbitt, N. W. Carlson, and T. W. Mossberg, "Real-time optical waveform convolver/cross correlator," Appl. Phys. Lett. **45**, 714–716 (1984).
10. K. D. Merkel, Z. Cole, and W. R. Babbitt, "Signal correlator with programmable variable time delay based on optical coherent transients," J. Lumin. **86**, 375–382 (2000).
11. F. Schlottau and K. H. Wagner, "Demonstration of a continuous scanner and time-integrating correlator using spatial-spectral holography," J. Lumin. **107**, 90–102 (2004).
12. K. D. Merkel, R. K. Mohan, Z. Cole, T. Chang, A. Olson, and W. R. Babbitt, "Multi-Gigahertz radar range processing of baseband and RF carrier modulated signals in Tm:YAG," J. Lumin. **107**, 62–74 (2004).
13. M. Tian, R. Reibel, and W. R. Babbitt, "Demonstration of optical coherent transient true-time delay at 4 Gbits/s," Opt. Lett. **26**, 1143–1145 (2001).

14. V. Lavielle, F. D. Seze, I. Lorgeré, and J.-L. Le Gouët, "Wideband radio frequency spectrum analyzer: improved design and experimental results," *J. Lumin.* **107**, 75–89 (2004).
15. R. K. Mohan, Z. Cole, R. R. Reibel, T. Chang, K. D. Merkel, W. R. Babbitt, M. Colice, F. Schlottau, and K. H. Wagner, "Microwave spectral analysis using optical spectral hole-burning," in *Proceedings of the IEEE International Topical Meeting on Microwave Photonics* (IEEE, 2004), pp. 24–27.
16. M. Colice, F. Schlottau, K. Wagner, R. K. Mohan, W. R. Babbitt, I. Lorgeré, and J.-L. Le Gouët, "RF Spectrum Analysis in Spectral Hole Burning Media," in *Optical Information Systems II*, B. Javidi and D. Psaltis, eds., *Proc. SPIE* **5557**, 132–139 (2004).
17. I. Lorgeré, L. Ménager, V. Lavielle, J.-L. Le Gouët, D. Dolfi, S. Tonda, and J.-P. Huignard, "Demonstration of a radio-frequency spectrum analyser based on spectral hole burning," *J. Mod. Opt.* **49**, 2459–2475 (2002).
18. M. Mitsunaga and R. G. Brewer, "Generalized perturbation theory of coherent optical emission," *Phys. Rev. A* **32**, 1605–1613 (1985).
19. V. Crozatier, V. Lavielle, F. Bretenaker, J. Le Gouët, and I. Lorgeré, "High-resolution radio frequency spectral analysis with photon echo chirp transform in an Er:YSO crystal," *IEEE J. Quantum Electron.* **40**, 1450–1457 (2004).
20. G. Gorju, V. Crozatier, I. Lorgeré, J.-L. Le Gouët, and F. Bretenaker, "10-GHz bandwidth rf spectral Analyzer with MHz resolution based on spectral hole burning in Tm³⁺:YAG," *IEEE Photon. Technol. Lett.* **17**, 2385–2387 (2005).
21. F. Schlottau, M. Colice, K. H. Wagner, and W. R. Babbitt, "Spectral hole burning for wideband, high-resolution radio-frequency spectrum analysis," *Opt. Lett.* **30**, 3003–3005 (2005).
22. D. T. Chen, H. R. Fetterman, A. T. Chen, W. H. Steier, L. R. Dalton, W. S. Wang, and Y. Q. Shi, "Demonstration of 110 GHz electro-optic polymer modulators," *Appl. Phys. Lett.* **70**, 3335–3337 (1997).
23. K. Noguchi, H. Miyazawa, and O. Mitomi, "Frequency-dependent propagation characteristics of coplanar waveguide electrode on 100 GHz Ti:LiNbO₃ optical modulator," *Electron. Lett.* **34**, 661–663 (1998).
24. M. Colice, F. Schlottau, and K. Wagner, "Ultrawideband, wide-open rf spectrum analysis using spectral hole burning," in *Microwave Photonics*, J. Yao, ed., *Proc. SPIE* **5971**, 564–573 (2005).
25. P. Meystre and M. Sargent III, *Elements of Quantum Optics*, 2nd ed. (Springer-Verlag, 1991).
26. L. Allen and J. H. Eberly, *Optical Resonance and Two-Level Atoms* (Dover, 1987).
27. A. Papoulis, *Systems and Transforms with Applications in Optics* (McGraw-Hill, 1968).
28. M. A. Poletti, "Linearly swept frequency measurements and the Wigner–Ville distribution," in *Time-Frequency Signal Analysis: Methods and Applications*, B. Boashash, ed., (Longman Cheshire, 1992), Chap. 19, pp. 424–444.
29. M. A. Poletti, "Linearly swept frequency measurements, time-delay spectrometry, and the Wigner distribution," *J. Audio Eng. Soc.* **36**, 457–468 (1988).
30. T. Chang, M. Tian, R. K. Mohan, C. Renner, K. D. Merkel, and W. R. Babbitt, "Recovery of spectral features readout with frequency chirped laser fields," *Opt. Lett.* **30**, 1129–1131 (2005).
31. G. Hok, "Response of linear resonant systems to excitation of a frequency varying linearly with time," *J. Appl. Phys.* **19**, 242–250 (1948).
32. W. R. Babbitt and R. Krishna Mohan, Spectrum Lab, Department of Physics, Montana State University, Bozeman, Montana 59717 (personal communication, 2005).
33. J. Huang, J. M. Zhang, A. Lezama, and T. W. Mossberg, "Excess dephasing in photon-echo experiments arising from excitation-induced electronic level shifts," *Phys. Rev. Lett.* **63**, 78–81 (1989).
34. S. Kröll, E. Y. Xu, M. K. Kim, M. Mitsunaga, and R. Kachru, "Intensity-dependent photon-echo relaxation in rare-earth-doped crystals," *Phys. Rev. B* **41**, 11568–11571 (1990).
35. M. Mitsunaga, T. Takagahara, R. Yano, and N. Uesegi, "Excitation-induced frequency shift probed by stimulated photon echoes," *Phys. Rev. Lett.* **68**, 3216–3219 (1992).
36. G. K. Liu and R. L. Cone, "Laser-induced instantaneous spectral diffusion in Tb³⁺ compounds as observed in photon-echo experiments," *Phys. Rev. B* **41**, 6193–6200 (1990).
37. G. W. Burr, T. L. Harris, W. R. Babbitt, and C. M. Jefferson, "Incorporating excitation-induced dephasing into the Maxwell–Bloch numerical modeling of photon echoes," *J. Lumin.* **107**, 314–331 (2004).
38. T. Böttger, C. W. Thiel, Y. Sun, and R. L. Cone, "Optical decoherence and spectral diffusion at 1.5 μm in Er³⁺:Y₂SiO₅ versus magnetic field, temperature, and Er³⁺ concentration," *Phys. Rev. B* **73**, 075101 (2006).
39. A. Szaabo and R. Kaarli, "Optical hole burning and spectral diffusion in ruby," *Phys. Rev. B* **44**, 12307–12313 (1991).
40. G. Armagan, A. M. Buoncristiani, and B. D. Bartolo, "Excited state dynamics of thulium ions in yttrium aluminum garnets," *Opt. Mater.* **1**, 11–20 (1992).
41. C. J. Karlsson and F. A. A. Olsson, "Linearization of the frequency sweep of a frequency-modulated continuous-wave semiconductor laser radar and the resulting ranging performance," *Appl. Opt.* **38**, 3376–3386 (1999).
42. G. Gorju, V. Crozatier, V. Lavielle, I. Lorgeré, J.-L. Le Gouët, and F. Bretenaker, "Experimental investigation of deterministic and stochastic frequency noises of a rapidly frequency chirped laser," *Eur. Phys. J. Appl. Phys.* **30**, 175–183 (2005).
43. N. M. Strickland, P. B. Sellin, Y. Sun, J. L. Carlsten, and R. L. Cone, "Laser stabilization using regenerative spectral hole burning," *Phys. Rev. B* **62**, 1473–1476 (2000).
44. G. C. Bjorklund, M. D. Levenson, W. Lenth, and C. Ortiz, "Frequency modulation FM spectroscopy," *Appl. Phys. B* **32**, 145–152 (1983).
45. R. W. P. Drever, J. L. Hall, F. V. Kowalski, J. Hough, G. M. Ford, A. J. Munley, and H. Ward, "Laser phase and frequency stabilization using an optical resonator," *Appl. Phys. B* **31**, 97–105 (1983).
46. K. S. Repasky and J. L. Carlsten, "Simple method for measuring frequency chirps with a Fabry–Perot interferometer," *Appl. Opt.* **39**, 5500–5504 (2000).
47. K. H. Wagner, F. Schlottau, and J. Bregman, "Array imaging using spatial-spectral holography," in *Optics in Computing* (International Commission on Optics, 2002).
48. F. Schlottau, K. Wagner, J. Bregman, and J.-L. Le Gouët, "Sparse antenna array multiple beamforming and spectral analysis using spatial-spectral holography," in *IEEE International Topical Meeting on Microwave Photonics* (IEEE, 2003), pp. 355–358.
49. F. Schlottau, B. Braker, and K. Wagner, "Squint compensation for a broadband RF array spectral imager using spatial spectral holography," in *Imaging Spectrometry X*, S. S. Shen and P. E. Lewis, eds., *Proc. SPIE* **5546**, 244–252 (2004).
50. B. M. Braker, Y. Li, D. Gu, F. Schlottau, and K. H. Wagner, "Broadband microwave imaging with spectral hole burning for squint compensation," in *Passive Millimeter-Wave Imaging Technology VIII*, R. Appleby and D. A. Wikner, eds., *Proc. SPIE* **5789**, 69–79 (2005).